

---

---

# Feasibility of $^{18}\text{F}$ -Fluoromisonidazole Kinetic Modeling in Head and Neck Cancer Using Shortened Acquisition Times

Milan Grkovski<sup>1</sup>, Jazmin Schwartz<sup>1</sup>, Mithat Gönen<sup>2</sup>, Heiko Schöder<sup>3</sup>, Nancy Y. Lee<sup>4</sup>, Sean D. Carlin<sup>3</sup>, Pat B. Zanzonico<sup>1</sup>, John L. Humm<sup>1</sup>, and Sadek A. Nehmeh<sup>1</sup>

<sup>1</sup>Department of Medical Physics, Memorial Sloan Kettering Cancer Center, New York, New York; <sup>2</sup>Department of Epidemiology-Biostatistics, Memorial Sloan Kettering Cancer Center, New York, New York; <sup>3</sup>Department of Radiology, Memorial Sloan Kettering Cancer Center, New York, New York; and <sup>4</sup>Department of Radiation Oncology, Memorial Sloan Kettering Cancer Center, New York, New York

---

$^{18}\text{F}$ -fluoromisonidazole dynamic PET (dPET) is used to identify tumor hypoxia noninvasively. Its routine clinical implementation, however, has been hampered by the long acquisition times required. We investigated the feasibility of kinetic modeling using shortened acquisition times in  $^{18}\text{F}$ -fluoromisonidazole dPET, with the goal of expediting the clinical implementation of  $^{18}\text{F}$ -fluoromisonidazole dPET protocols. **Methods:** Six patients with squamous cell carcinoma of the head and neck and 10 HT29 colorectal carcinoma-bearing nude rats were studied. In addition to an  $^{18}\text{F}$ -FDG PET scan, each patient underwent a 45-min  $^{18}\text{F}$ -fluoromisonidazole dPET scan, followed by 10-min acquisitions at  $96 \pm 4$  and  $163 \pm 17$  min after injection. Ninety-minute  $^{18}\text{F}$ -fluoromisonidazole dPET scans were acquired in animals. Intratumor voxels were classified into 4 clusters based on their kinetic behavior using k-means clustering. Kinetic modeling was performed using the foregoing full datasets (FD) and repeated for each of 2 shortened datasets corresponding to the first approximately 100 min (SD1; patients only) or the first 45 min (SD2) of dPET data. The kinetic rate constants (KRCs) as calculated with a 2-compartment model for both SD1 and SD2 were compared with those derived from FD by correlation (Pearson), regression (Passing-Bablok), deviation (Bland-Altman), and classification (area-under-the-receiver-operating characteristic curve) analyses. Simulations were performed to assess uncertainties due to statistical noise. **Results:** Strong correlation ( $r \geq 0.75$ ,  $P < 0.001$ ) existed between all KRCs deduced from both SD1 and SD2, and from FD. Significant differences between KRCs were found only for FD-SD2 correlations in patient studies.  $K_1$  and  $k_3$  were reproducible to within approximately 6% and approximately 30% (FD-SD1; patients) and approximately 4% and approximately 75% (FD-SD2; animals). Area-under-the-receiver-operating characteristic curve values for classification of patient clusters as hypoxic, using a tumor-to-blood ratio greater than 1.2, were 0.91 (SD1) and 0.86 (SD2). The percentage SD in estimating  $K_1$  and  $k_3$  from 45-min shortened datasets due to noise was less than 1% and between 2% and 12%, respectively. **Conclusion:** Using single-session 45-min shortened  $^{18}\text{F}$ -fluoromisonidazole dPET datasets appears to be adequate for the identification of intratumor regions of hypoxia. However,  $k_3$  was significantly overestimated in the clinical cohort. Further studies are necessary to evaluate the clinical significance of differences between the results as calculated from full and shortened datasets.

**Key Words:** dynamic PET; hypoxia;  $^{18}\text{F}$ -fluoromisonidazole; kinetic modeling

**J Nucl Med 2016; 57:334–341**  
DOI: 10.2967/jnumed.115.160168

---

**T**he relationship between tumor hypoxia and poor overall outcome has been demonstrated for several types of human malignancies (1), including head and neck cancer (2–4). Tumor hypoxia can be identified by measuring partial pressure of oxygen using polarographic electrodes (3,5). Another method to characterize tumor hypoxia is by means of immunohistochemical analysis of exogenous (e.g., pimonidazole, etanidazole pentafluoride) or endogenous (e.g., carbonic anhydrase IX, hypoxia-inducible factor 1 $\alpha$ ) hypoxia markers (6). Both techniques, however, are invasive, require lesions accessible to needle placement, and are subject to undersampling.

PET with  $^{18}\text{F}$ -fluoromisonidazole is a noninvasive imaging technique that has been shown to be clinically feasible for detecting tumor hypoxia (7,8). Because of its lipophilicity,  $^{18}\text{F}$ -fluoromisonidazole passively diffuses out of the vasculature and through cell membranes and is reduced to a nondiffusible charged form by intracellular nitroreductases (7). Under normoxic conditions, the reduced form of fluoromisonidazole is rapidly oxidized back to its diffusible form, with tissue levels rapidly declining as blood-borne fluoromisonidazole is cleared. Otherwise, the fluoromisonidazole metabolites remain trapped and undergo irreversible reductions to form covalent bonds to macromolecules, leading to progressive accumulation of  $^{18}\text{F}$  within hypoxic cells (7). Previous studies suggested a tumor-to-blood ratio in excess of 1.4 at 2 plus hours after injection to identify hypoxic volumes (7,8). However, a combination of severely hypoxic and necrotic tissues supplied by structurally and functionally abnormal vasculature may lead to low total uptake even at late time points. Conversely, the physiologic clearance of  $^{18}\text{F}$ -fluoromisonidazole from well-perfused normoxic tissue may result in measured activity concentrations comparable to those in hypoxic tumors (9,10). To overcome the foregoing limitations in the interpretation of static  $^{18}\text{F}$ -fluoromisonidazole images, kinetic modeling of dynamic PET (dPET) data has been suggested as a means of reliably characterizing perfusion and identifying hypoxia in tumors (9,10).

A major drawback of such an approach is the long acquisition times typically used to extract the pharmacokinetic parameters of

---

Received May 26, 2015; revision accepted Nov. 11, 2015.  
For correspondence or reprints contact: Milan Grkovski, Department of Medical Physics, Memorial Sloan Kettering Cancer Center, 1275 York Avenue, New York, NY 10065.  
E-mail: grkovskm@mkscc.org  
Published online Nov. 25, 2015.  
COPYRIGHT © 2016 by the Society of Nuclear Medicine and Molecular Imaging, Inc.

<sup>18</sup>F-fluoromisonidazole. At our institution, the <sup>18</sup>F-fluoromisonidazole dPET protocol consists of 30- to 45-min dPET followed by 10-min static PET acquisitions at approximately 90 min and at approximately 150–180 min after injection. Such lengthy protocols compromise clinical practicality as well as patient compliance and accrual. The aim of the current study was to assess the reproducibility of kinetic rate constants (KRCs) as calculated from shortened <sup>18</sup>F-fluoromisonidazole dPET datasets in a cohort of patients with squamous cell carcinoma of the head and neck (SCCHN) and in a preclinical rodent model. Special attention was paid to kinetic rate constants serving as surrogate metrics of perfusion ( $K_1$ ) and hypoxia ( $k_3$ ).

## MATERIALS AND METHODS

### Clinical Studies

This retrospective study was approved by our Institutional Review Board (IRB 04-070; registered under www.clinicaltrials.gov identifier NCT00606294), and all subjects signed a written informed consent form regarding the examination and use of anonymous data for research and publication purposes. Patients aged 18 years or older with a histologically confirmed diagnosis of SCCHN were eligible for this study. Exclusion criteria included all nasopharyngeal, paranasal sinus, salivary cancer, and thyroid malignancies; prior chemotherapy or radiotherapy within the last 3 y; previous surgical resection for the same disease; any prior radiotherapy to the head and neck region; and pregnancy.

Six male patients (age,  $59 \pm 10$  y) were included in the study (Table 1). All patients were scanned on a flat-top couch insert in a radiotherapy treatment immobilization mask. Intravenous lines in contralateral antecubital veins were inserted for each patient and were used for radiotracer injection.

**<sup>18</sup>F-FDG PET/CT Protocol.** Each patient underwent a baseline <sup>18</sup>F-FDG PET/CT study for radiotherapy simulation. Patients were injected intravenously with  $451 \pm 18$  MBq of <sup>18</sup>F-FDG (range, 437–477 MBq), after a fasting period of 6 h or more. Whole-body PET scans were acquired for 3 min per bed position (70-cm field of view [FOV]), starting at  $69 \pm 10$  min (range, 61–84 min) after injection. Data were acquired on a Discovery STE PET/CT scanner (GE Healthcare Inc.), having a resolution of approximately 5.5 mm in full width at half maximum at the center of the FOV. The CT images were acquired with oral contrast using the following settings: 140 kVp, 250 mA, and 3.8-mm slice thickness. PET emission data were corrected for attenuation, scatter, and random events and then iteratively

reconstructed into a  $256 \times 256 \times 47$  matrix (voxel dimensions,  $2.73 \times 2.73 \times 3.27$  mm) using the ordered subset expectation maximization algorithm provided by the manufacturer (2 iterations, 20 subsets, and a gaussian postprocessing filter of 6.0 mm in full width at half maximum).

**<sup>18</sup>F-Fluoromisonidazole PET/CT Protocol.** Each patient underwent <sup>18</sup>F-fluoromisonidazole dPET imaging on a Discovery STE PET/CT scanner 1–3 d after the <sup>18</sup>F-FDG PET/CT. <sup>18</sup>F-fluoromisonidazole was prepared as previously reported (11). Patients received an intravenous bolus injection of  $429 \pm 41$  MBq of <sup>18</sup>F-fluoromisonidazole (range, 364–475 MBq). The dPET acquisition was initiated simultaneously with the injection. <sup>18</sup>F-fluoromisonidazole data were acquired in list-mode for 1 bed position, centered over the lesion, for 45 min (binned into  $6 \times 30$ ,  $7 \times 60$ , and  $7 \times 300$  s frames). Two additional 10-min static image sets were acquired at  $96 \pm 4$  min (range, 90–103 min) and  $163 \pm 17$  (range, 150–186 min) after injection. Patients were allowed a rest period between scans. Before each PET scan, a low-dose CT scan was obtained for attenuation correction and image registration purposes. CT scans were obtained with 120 kVp; 3.8-mm slice thickness; and 40, 10, and 80 mA for the first, second, and third scans, respectively. List-mode PET data of the first 3 min of the dataset was retrospectively rebinned into  $36 \times 5$  s frames to delineate the carotid artery from the internal jugular vein and thereby define the input function (IF) volume of interest (VOI). All <sup>18</sup>F-fluoromisonidazole PET images were reconstructed using the same parameters as for the <sup>18</sup>F-FDG study.

### Preclinical Studies

All animal experiments and procedures were approved by our Institutional Animal Care and Use Committee and complied with the National Institutes of Health regulations on the research use of rodents.

Ten rats were included in this study. HT29 human colorectal carcinoma cells (no. HTB-38; American Type Culture Collection) were maintained in Dulbecco modified Eagle medium (MediaTech Inc.) supplemented with 10% fetal bovine serum and 1% penicillin–streptomycin at 37°C in a 5% CO<sub>2</sub> atmosphere. Xenografts were initiated by subcutaneous inoculation of approximately  $5.0 \times 10^6$  cells in 0.2 mL of phosphate-buffered saline into the right hind limb of each of ten 6- to 8-wk-old female athymic *nu/nu* rats as previously described (12). Animals (weight,  $228 \pm 18$  g) were anesthetized using 2% isoflurane in air. An activity of  $41.3 \pm 2.9$  MBq (range, 36.7–46.0 MBq) of <sup>18</sup>F-fluoromisonidazole was administered via tail vein injection. Image acquisition was performed with either an R4 or Focus 120 microPET scanner (Siemens Medical Solutions Inc.), with animals prone and the FOV centered on the tumor, using a 350- to 700-keV

**TABLE 1**  
Patient Characteristics

Patient no.	Tumor stage	Tumor site	Lesion	Lesion VOI (cm <sup>3</sup> )
1	cT1N2b	Left glossal tonsillar sulcus and left base of tongue	1	13.3
			2	3.3
2	T1N2b	Left tonsil	3	24.2
3	cT2N3M0	Left tonsil	4	3.3
4*	cT2N2b	Base of tongue	5	32.9
5†	cT3N2a	Left tonsil and bilateral neck	6	33.0
			7	6.5
6*	T2N2b	Left tonsil	8	11.2

\*Patients for whom list-mode data were not available.

†Patient whose first <sup>18</sup>F-fluoromisonidazole acquisition was stopped at 40 min.

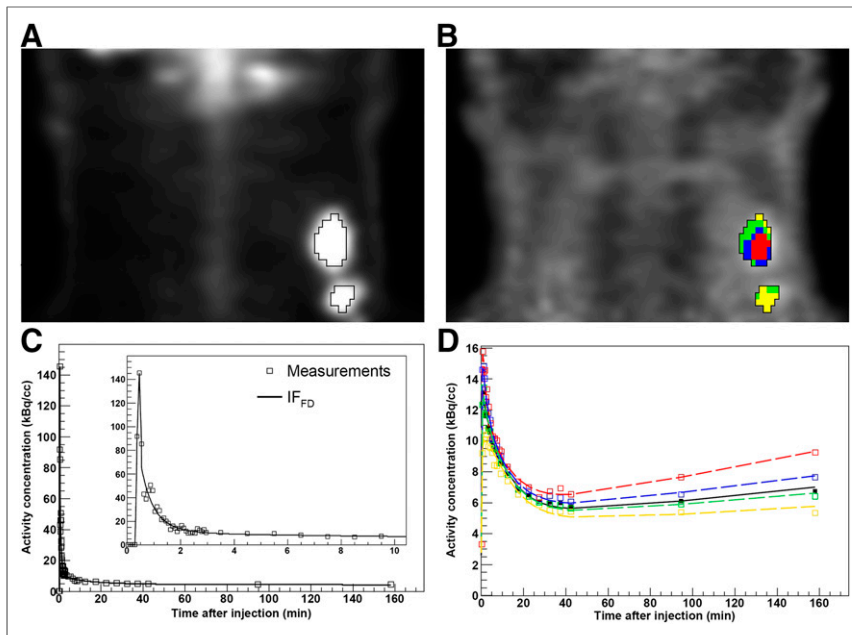


**FIGURE 1.** Clinical study of patient 1 (lesion 1). (A) Definition of VOI (wVOI) on  $^{18}\text{F}$ -FDG PET image (coronal view). (B) wVOI is copied to coregistered  $^{18}\text{F}$ -fluoromisonidazole dPET image and subclassified into 4 clusters (cVOIs). (C) Modeled input function based on full dataset ( $\text{IF}_{\text{FD}}$ ), superimposed on measurements. Insert shows initial 10 min of data. (D) Modeled time-activity curves derived from wVOI (solid line) and from 4 cVOIs (dashed lines), superimposed on measured wVOI time-activity curve (■) and cVOI time-activity curves (□). cVOIs are color-coded to those shown in B.

energy window and 6-ns coincidence timing window. Data were acquired in dynamic mode for a total of 90 min and binned into  $4 \times 5$ ,  $4 \times 10$ ,  $4 \times 30$ ,  $7 \times 60$ ,  $10 \times 300$ , and  $3 \times 600$  s frames. Images were reconstructed using a 3-dimensional maximum a posteriori estimation algorithm into a  $128 \times 128 \times 95$  matrix (voxel dimensions,  $0.87 \times 0.87 \times 0.79$  mm). The reconstructed image resolution was approximately 1.6 mm in full width at half maximum at the center of the FOV. Measurements performed with a uniformly filled phantom of dimensions comparable to a rat demonstrated adequate uniformity without attenuation and scatter correction. Therefore, no attenuation or scatter correction was applied for the rat image data.

### Image Analysis

Reconstructed dPET images were analyzed with PMOD (version 3.504; PMOD Technologies GmbH). For patient studies, 8 lesions were identified on the  $^{18}\text{F}$ -FDG PET/CT scans. In 1 case (patient 5), dynamic  $^{18}\text{F}$ -fluoromisonidazole acquisition was interrupted at 40 min after injection because of the patient's discomfort and inability to continue. The 2 delayed  $^{18}\text{F}$ -fluoromisonidazole and the  $^{18}\text{F}$ -FDG image sets were spatially registered to the first  $^{18}\text{F}$ -fluoromisonidazole image set using the General Registration tool in the AW Workstation (version 4.6; GE Healthcare). Rigid image registration was performed locally for each lesion using the CT image sets, and the resulting transformation matrices were applied to the corresponding PET image sets. The whole-tumor VOI (wVOI) was delineated on  $^{18}\text{F}$ -FDG images using a 50% of the maximum tumor activity concentration threshold, and the resulting VOI was copied to the corresponding dynamic  $^{18}\text{F}$ -fluoromisonidazole image set. For animal studies, the wVOI was delineated manually on a slice-by-slice basis using the final frame (80–90 min).

### Kinetic Modeling

Kinetic modeling of  $^{18}\text{F}$ -fluoromisonidazole dPET images was performed in PMOD, using an irreversible 1-plasma 2-tissue-compartment

model (13). In this model,  $C_p(t)$ ,  $C_1(t)$ , and  $C_2(t)$  correspond to the activity concentration as a function of time after injection in the plasma ( $C_p(t)$ ), in the form of free and otherwise nonhypoxia-localized activity in tissue ( $C_1(t)$ ), and in the form of hypoxia-localized tracer ( $C_2(t)$ ). The 4 unknowns estimated are  $v_B$ , the fractional vascular volume;  $K_1$ , the transfer rate constant from  $C_p$  to  $C_1$ ;  $K_1/k_2$ , the distribution volume of  $C_1$ ; and  $k_3$ , the rate of conversion from  $C_1$  to  $C_2$ .  $k_4$  was set to 0, assuming irreversible trapping of  $^{18}\text{F}$ -fluoromisonidazole (7). Although  $v_B$  and  $K_1/k_2$  are unitless,  $K_1$  and  $k_3$  (assuming unit density tissue) are expressed in  $\text{min}^{-1}$ .

For patient studies, the input function was derived by segmenting the common carotid artery on the rebinned dPET dataset (i.e., corresponding to the  $36 \times 5$  s time frames). In 2 cases (patients 4 and 6), the list-mode data were not available; because the common carotid artery could not be identified from the original dPET dataset, the IF VOI was defined on the internal jugular vein. For animal studies, the input function was derived by segmenting the descending aorta (identified from a summed image of the first 3 frames [15 s] of the study). All IF time-activity curves were corrected for partial-volume effect by calculating the geometric transfer matrix containing weighting elements

$w_{i,j}$  that represent the fraction of true activity spilled over from  $\text{VOI}_i$  into  $\text{VOI}_j$  (14). Neighboring regions were defined using k-means clustering based on the time-weighted Euclidean distance between the voxel time-activity curves (10 clusters, 200 iterations) (15).

Voxels within each wVOI were similarly subclassified into 4 clusters, with k-means clustering performed based on the first 45 min of dPET data. The choice of 4 tumor subvolumes (cVOIs) was made to conceptually represent hypoxic, partially hypoxic, normoxic, and necrotic regions of the tumor. The Levenberg–Marquardt algorithm (16) was used to fit the cVOI-derived time-activity curves to estimate the KRCs (100 random fits, 200 iterations). The target activity concentration at each time frame was weighed by (13):

$$w_i = \frac{1}{\sigma_i^2}, \sigma_i = c \sqrt{\left( \frac{\text{AC}(t_i)}{\Delta t_i \times e^{-\lambda t_i}} \right)}, \quad \text{Eq. 1}$$

where  $c$  is the scaling factor,  $\Delta t_i$  is the frame duration,  $\text{AC}(t_i)$  is the decay-corrected activity concentration measured at the midframe time  $t_i$ , and  $\lambda = \ln 2 / T_{1/2}$  is the isotope decay constant. Kinetic modeling was conducted for the full dataset (FD; reference standard), the first approximately 100 min of dPET data (SD1; patients only), and the first 45 min of dPET data (SD2). The input function time-activity curves that were corrected for partial-volume effect were fitted with a 3-term exponential function, using the available temporal data in each case, to obtain a modeled IF as:

$$\text{IF}(t) = \begin{cases} \text{Linear interpolation} & t < t_0 \\ \sum_{i=1}^3 A_i e^{-(t-t_0)\ln 2/T_i} & t \geq t_0 \end{cases}, \quad \text{Eq. 2}$$

where  $\text{IF}(t)$  is the modeled activity concentration in the blood at time  $t$ ,  $t_0$  defines at what time the model switches from linear to triexponential

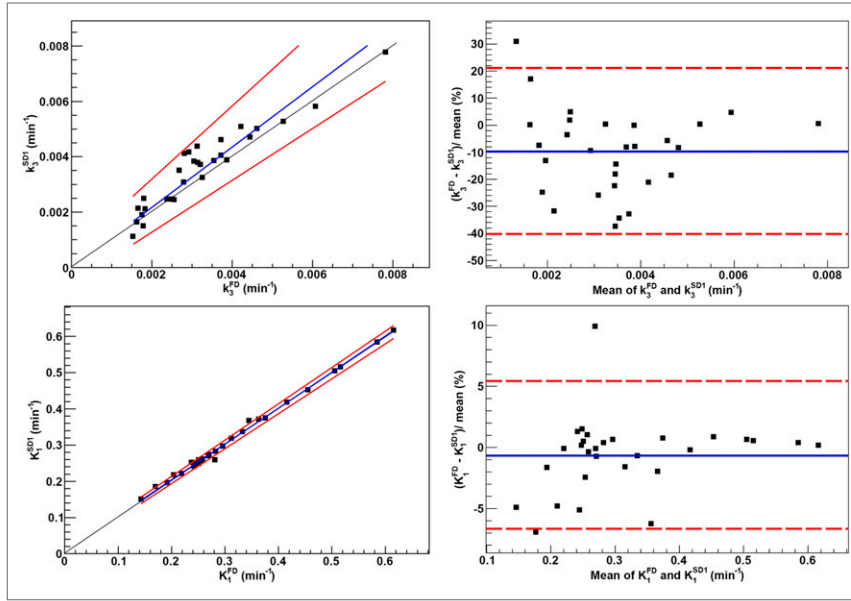


**FIGURE 2.** Passing–Bablok regression (left) and Bland–Altman analysis (right) results for  $k_3$  (top) and  $K_1$  (bottom), calculated using full (FD;  $\sim 170$  min) and  $\sim 100$  min shortened (SD1) datasets in clinical studies ( $n = 29$ ). Also displayed are regression line (blue) and its CIs (red) for Passing–Bablok regression and mean percentage difference (blue) with limits of agreement (red) for Bland–Altman analysis.

interpolation between measured values (after the IF peak), and the  $A_i$  and  $T_i$  terms represent the fitting parameters.

### Statistical Analysis

The kinetic rate constants calculated from each of the 2 shortened datasets were compared with those derived from the full dataset in a stepwise approach. First, a Pearson correlation coefficient ( $r$ ) was computed to calculate the strength and direction of a linear relationship between the KRCs, modeled as:

$$Y = \alpha + \beta X + \varepsilon, \quad \text{Eq. 3}$$

where intercept  $\alpha$ , slope  $\beta$ , and  $\varepsilon$  correspond to the systematic, proportional, and random differences. If a strong significant correlation ( $r \geq 0.75$ ,  $P < 0.05$ ) was found, nonparametric Passing–Bablok regression (17) was performed to test for the presence of systematic (95% confidence interval [CI] for  $\alpha$  does not include 0) or proportional (95% CI for  $\beta$  does not include 1) differences between the 2 sets of KRCs. A cumulative sum test for linearity was used to validate the applicability of Passing–Bablok analysis (17). Random differences

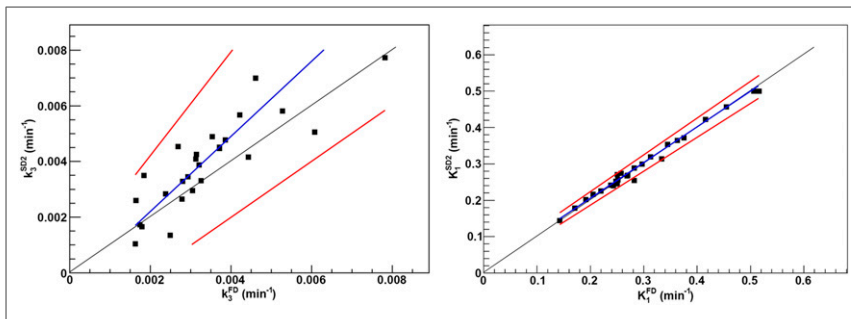


**FIGURE 3.** Passing–Bablok regression results for  $k_3$  (left) and  $K_1$  (right), calculated using full (FD;  $\sim 170$  min) and 45 min shortened (SD2) datasets in clinical studies ( $n = 26$ ). Also displayed are regression line (blue) and its CIs (red).

between 2 sets of KRCs were measured using residual SD. If the slope and intercept were not significantly different from 1 and 0, respectively, Bland–Altman analysis (18) was performed to calculate the 95% limits of agreement, after testing for the normality assumption on the differences between 2 sets of KRCs using the Kolmogorov–Smirnov test.

Receiver-operating-characteristics analysis (19) was performed in patient studies to evaluate the reliability of shortened datasets for the task of identifying tumor hypoxia, using a tumor-to-blood ratio greater than 1.2 (4) as a discrimination threshold. The diagnostic performance was assessed on the basis of  $k_3$  and  $K_i$  (influx rate constant, defined as  $K_1 k_3 / [k_2 + k_3]$ , in units of  $\text{min}^{-1}$ ) calculated from shortened datasets, and the area-under-the-receiver-operating characteristics curve was subsequently determined (19). All statistical analyses were performed in MedCalc (version 15.6; MedCalc Software bvba).

### Simulations

Modeled time–activity curves (mTACs) were obtained by fitting all 32 cVOI-derived time–activity curves from patients. For each mTAC, 100 samples of noisy time–activity curves were simulated by adding noise consistent to that observed on a cluster level. The noise was estimated as follows: data were acquired on a Discovery STE PET/CT scanner using a National Electrical Manufacturers Association/International Electrotechnical Commission body phantom filled with  $^{18}\text{F}$ -FDG (activity concentration was equivalent to the average tumor  $^{18}\text{F}$ -fluoromisonidazole activity concentration in the  $\sim 170$ -min time point), for 30 min in gated mode (10 bins), as described previously (20). Images were reconstructed using the same parameters as in clinical studies. Fifty nonoverlapping VOIs of  $5 \times 5 \times 5$  voxels (corresponding in size to the average patients' cluster volumes) were drawn on the central axial plane in the phantom image set. For each VOI, a histogram of the average activity concentrations from the 10 gated image bins was constructed and fitted with a normal distribution fit, to calculate the SD of the distribution and deduce the corresponding scaling factor  $c$  (as per Eq. 1). The average scaling factor over 50 VOIs was subsequently used to simulate cluster noise on a frame-by-frame basis for each mTAC. Kinetic modeling was conducted using mTACs and input functions as derived from full datasets (mTAC<sub>FD</sub> and IF<sub>FD</sub>; that is, for SD1 and SD2, mTAC<sub>FD</sub> and IF<sub>FD</sub> were truncated). The percentage bias and percentage SD were calculated with respect to the true value for each kinetic parameter (13):

$$\%bias_i = \left( \frac{\mu_{x_i}}{x_i^{true}} - 1 \right) \times 100, \quad \text{Eq. 4}$$

$$\%stddev_i = \left( \frac{\sigma_{x_i}}{x_i^{true}} \right) \times 100, \quad \text{Eq. 5}$$

where  $\mu_{x_i}$ ,  $\sigma_{x_i}$ , and  $x_i^{true}$  are the sample mean, sample SD, and true value of a kinetic parameter  $x$  for  $i$ -th cluster. Additionally, Pearson  $r$  was calculated for  $K_1$  and  $k_3$  deduced from the 100 noisy time–activity curves using FD and SD1 and SD2, respectively.

**TABLE 2**  
Summary of Correlation, Regression, and Deviation Analyses

Dataset combination	KRC	Pearson $r$ (95% CI)	Passing-Bablok			Bland-Altman			
			$P^*$	Slope (95% CI)	Intercept (95% CI)	Residual SD (95% CI)	$P^\dagger$	Mean % difference (95% CI)	95% limits of agreement (lower; upper)
FD-SD1 (clinical) $n = 29$	$k_3$	0.95 (0.89–0.98)	0.58	1.08 (0.94–1.32)	-6.0E-6 (-6.1E-4 to 5.3E-4)	3.4E-4 (-6.7E-4 to 6.7E-4)	0.20	-10 (-16 to -4)	-40; 21
	$K_1$	1.00 (0.99–1.00)	0.58	0.99 (0.97–1.00)	0.0045 (-1.3E-4 to 0.011)	0.0058 (-0.011 to 0.011)	1.00	-1 (-2 to 1)	-7; 5
FD-SD2 (clinical) $n = 26$	$k_3$	0.85 (0.69–0.93)	1.00	1.40 (1.01–1.86)	-6.8 E-4 (-0.0020 to 4.7E-4)	6.3E-4 (-0.0012 to 0.0012)	Analysis not conducted	Analysis not conducted	Analysis not conducted
	$K_1$	1.00 (0.99–1.00)	0.86	1.04 (0.99–1.08)	-0.012 (-0.024 to 2.2E-4)	0.0060 (-0.012 to 0.012)	1.00	0 (-2 to 1)	-8; 7
FD-SD2 (preclinical) $n = 21$	$k_3$	0.91 (0.79–0.96)	0.98	1.10 (0.89–1.38)	5.2E-4 (-5.1E-4 to 0.0013)	8.2E-4 (-0.0016 to 0.0016)	0.82	-26 (-43 to -8)	-100; 49
	$K_1$	1.00 (0.99–1.00)	0.98	1.02 (0.98–1.06)	-0.0013 (-0.0079 to 0.0069)	0.0038 (-0.0075 to 0.0075)	1.00	-1 (-2 to 0)	-5; 3

\*Cumulative sum test.

†Kolmogorov–Smirnov test.

FD = full dataset (~170 min in clinical, 90 min in preclinical studies); SD1 = first shortened dataset (~100 min); SD2 = second shortened dataset (45 min).

**TABLE 3**  
Summary of Classification Analyses

Dataset	KRC	AUC (95% CI; binomial exact)	Associated criterion
SD1, $n = 32$	$k_3$	0.70 (0.51–0.85)	>0.0021
	$K_1$	0.91 (0.75–0.98)	>0.0027
SD2, $n = 32$	$k_3$	0.80 (0.62–0.92)	>0.0034
	$K_1$	0.86 (0.69–0.96)	>0.0023

AUC = area-under-the-receiver-operating characteristics curve; SD1 = first shortened dataset (~100 min); SD2 = second shortened dataset (45 min).

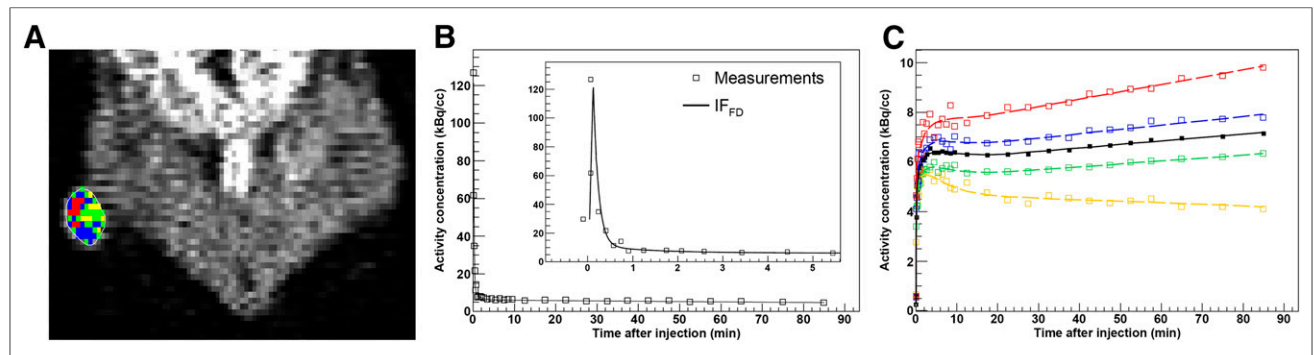


**FIGURE 4.** Kinetic modeling in tumor-bearing rodents (animal 1). (A) Definition of wVOI (white contour) on last 10-min frame of  $^{18}\text{F}$ -fluoromisonidazole dPET (coronal view), subclassified into 4 clusters (cVOIs). (B) Modeled input function based on full dataset ( $\text{IF}_{\text{FD}}$ ), superimposed on measured time–activity curves. Insert shows initial 5 min of data. (C) Modeled time–activity curves derived from wVOI (solid line) and from 4 cVOI (dashed lines), superimposed on measured wVOI time–activity curve (●) and cVOI time–activity curves (□). cVOIs are color-coded to those shown in A.

## RESULTS

### Clinical Studies

Coronal images for patient 1 are shown in Figures 1A ( $^{18}\text{F}$ -FDG PET) and 1B ( $^{18}\text{F}$ -fluoromisonidazole PET). The corresponding IF and tumor time–activity curves are shown in Figures 1C and 1D, respectively.

Clusters included  $25.0\% \pm 9.1\%$  of tumor voxels (range, 7.9%–46.0%). The KRCs calculated from the full dataset were  $0.0032 \pm 0.0015 \text{ min}^{-1}$  (range, 0.00071–0.0078  $\text{min}^{-1}$ ) for  $k_3$  and  $0.33 \pm 0.13 \text{ min}^{-1}$  (range, 0.13–0.62  $\text{min}^{-1}$ ) for  $K_1$ . Subsequently, only clusters that resulted in  $k_3 > 0.001 \text{ min}^{-1}$  (i.e., greater than the value

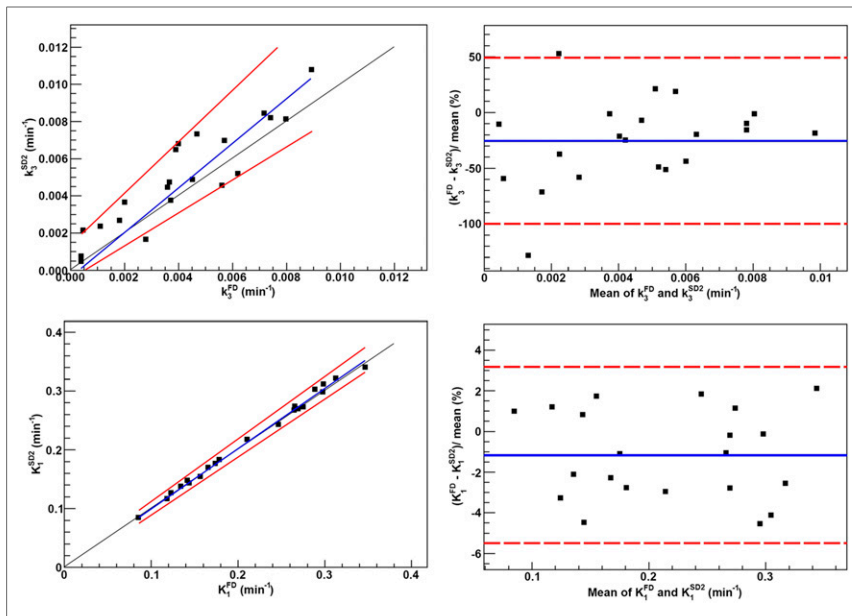


**FIGURE 5.** Passing–Bablok regression (left) and Bland–Altman analysis (right) results for  $k_3$  (top) and  $K_1$  (bottom), calculated using full (FD; 90 min) and 45 min shortened datasets (SD2) in preclinical studies ( $n = 21$ ). Also displayed are regression line (blue) and its CIs (red) for Passing–Bablok regression and mean percentage difference (blue) with limits of agreement (red) for Bland–Altman analysis.

reported for normoxic tumors and normal tissue in head and neck (13)) were included in the analysis, 29 clusters for SD1 and 26 clusters for SD2. The results of correlation, Passing–Bablok, and Bland–Altman analyses are summarized in Figure 2 (FD–SD1), Figure 3 (FD–SD2), and Table 2. Strong correlation ( $r \geq 0.75$ ,  $P < 0.001$ ) was observed between all corresponding KRCs. Passing–Bablok regression for FD–SD1 correlations showed no significant biases. Bland–Altman analysis revealed less than 1% and less than 10% mean differences between the calculated  $K_1$  and  $k_3$ , respectively, which were reproducible to within approximately 6% and approximately 30%. However, as proportional bias was observed when comparing FD–SD2, Bland–Altman analysis was not conducted. The analysis was repeated for  $K_i$  (data not shown), and no significant biases were identified.

The area-under-the-receiver-operating characteristics values for the classification of cVOIs as hypoxic are given in Table 3. Pearson  $r$  between tumor-to-blood ratio and  $k_3$  and  $K_i$ , as calculated using FD, were 0.71 and 0.90, respectively ( $P < 0.001$ ). For classification analyses, all 32 clusters were included.

### Preclinical Studies

A coronal image for animal 1 (lesion 1) is shown in Figure 4A, and the IF and tumor time–activity curves are shown in Figures 4B and 4C, respectively. The discontinuities in the example clusters may be due to noise propagated by the image reconstruction.

Clusters included  $25.0\% \pm 9.7\%$  of tumor voxels (range, 7.4%–44.2%). Twenty-one clusters were included in the analysis (excluding those for which  $k_3 = 0$ ). The KRCs calculated from the FD were  $0.0040 \pm 0.0026 \text{ min}^{-1}$  (range, 0.00041–0.0089  $\text{min}^{-1}$ ) for  $k_3$  and  $0.22 \pm 0.076 \text{ min}^{-1}$  (range, 0.085–0.35  $\text{min}^{-1}$ ) for  $K_1$ . The results of correlation, Passing–Bablok, and Bland–Altman analyses are summarized in Figure 5 and Table 2. Strong correlation was observed in all cases. Passing–Bablok analysis revealed no proportional or systematic biases. Bland–Altman analysis revealed less than 1% and less than 25%

mean differences between the calculated  $K_1$  and  $k_3$ , respectively, which were reproducible to within approximately 4% and approximately 75%.

Correction factor to the input function due to partial-volume effect for pooled data from both clinical and preclinical studies is higher at initial times after injection because of the largest differences between activity concentrations of  $^{18}\text{F}$ -fluoromisonidazole in vasculature and surrounding tissue, falling to approximately 1 as  $^{18}\text{F}$ -fluoromisonidazole diffuses from the vasculature (Fig. 6).

### Simulations

The average scaling factor  $c$  over the 50 VOIs was  $0.064 \pm 0.026$ . Although no bias was observed, the %stddev in  $k_3$  increased for shorter acquisition times and was inversely proportional to the true value of  $k_3$ , ranging from approximately 1%–4%, approximately 1%–6%, and approximately 2%–12% for FD, SD1, and SD2, respectively (Fig. 7). For  $K_1$ , both %bias and %stddev were less than 1% in all cases. Correlation between  $K_1$  as calculated using full and shortened noisy time–activity curves was strong ( $r > 0.90$ ), whereas for  $k_3$  it was lower ( $r = 0.55$

for SD1 and  $r = 0.19$  for SD2). A summary of simulation results is given in Table 4.

### DISCUSSION

dPET studies are largely confined to research applications, because the routine acquisition of multisession dPET scans is challenging. Despite reports that additional prognostic information such as the composite assessment of hypoxia and blood flow can be obtained from the analysis of  $^{18}\text{F}$ -fluoromisonidazole dPET data (21,22), static acquisitions at between 2 and 4 h after injection are predominantly used (23). We investigated the feasibility of kinetic modeling of  $^{18}\text{F}$ -fluoromisonidazole dPET using shortened acquisition times as a means of overcoming the limitations of both static and

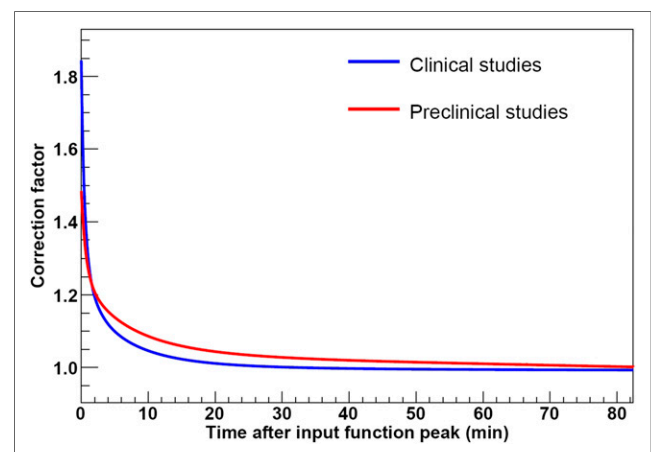


**FIGURE 6.** Correction factor for input function due to partial-volume effect, for pooled data from clinical and preclinical studies.

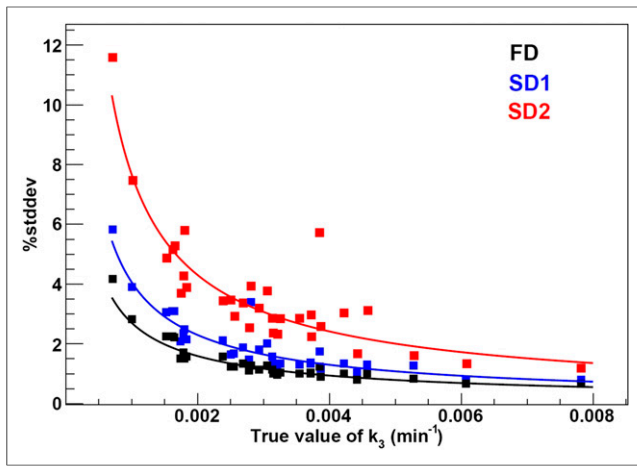


**FIGURE 7.** Percentage SD in estimating  $k_3$  from simulated data. FD = full dataset (~170 min); SD1 = first shortened dataset (~100 min); SD2 = second shortened dataset (45 min).

dynamic  $^{18}\text{F}$ -fluoromisonidazole imaging in identifying regions of tumor hypoxia in a clinically practical manner.

Measured uptake values on a voxel level exhibit considerable variations that represent not only differences in metabolic processes, but also noise, which is propagated through image reconstruction and kinetic modeling (10). Misregistration between the 3  $^{18}\text{F}$ -fluoromisonidazole scans may additionally compromise the accuracy of voxel-wise kinetic modeling. Clustering was performed to reduce these effects, while maintaining the ability to study hypoxia and perfusion characteristics of tumor subvolumes.

Strong correlations were found between all corresponding KRCs as calculated using shortened and full datasets (Table 2). In the clinical studies, Passing–Bablok regression revealed no significant differences between the KRCs as calculated from the FD and SD1, implying that using the approximately 100-min shortened datasets would not result in a bias in the estimation of KRCs. However, proportional differences were observed for FD–SD2 correlations. An increased residual SD with larger 95% CIs was also measured, showing that kinetic modeling of  $^{18}\text{F}$ -fluoromisonidazole dPET in SCCHN patients will be more prone to errors in determining the KRCs as the duration of the study is further shortened. In contrast, the results from the animal studies revealed no significant differences in the KRCs calculated from SD2 datasets. Narrower 95% CIs for slope, intercept, and residual SD were observed for KRCs calculated from the 45-min datasets in the animal compared with patient studies.

Results indicate that  $k_3$  was overestimated when using shortened datasets. Analyzing kinetically heterogeneous regions with a compartment model designed for homogeneous tissues may result in the overestimation of  $k_3$ , the magnitude of which depends on the acquisition period (24,25). Although this effect has been observed previously (26–28), further investigations are necessary to understand its significance in the context of  $^{18}\text{F}$ -fluoromisonidazole dPET.

Causes for the differences in the results between patient and animal studies may be attributed to a variety of factors including the more rapid circulation time and metabolism in rodents compared with man, dissimilarity of pharmacokinetic characteristics of  $^{18}\text{F}$ -fluoromisonidazole in the 2 tumor types, different acquisition lengths for full datasets, the fact that the animals were anesthetized during the acquisition whereas the patients were not, and the increased uncertainty brought about by the need to coregister the piecewise acquisition in human studies. Additionally, list-mode PET data were not available for 2 patients. Thirty-second initial time frames were therefore used, resulting in a lower peak activity concentration of the IF, leading to less stable KRC estimates (13).

The area-under-the-receiver-operating characteristics, calculated to assess the reliability of shortened  $^{18}\text{F}$ -fluoromisonidazole dPET datasets for the task of identifying tumor hypoxia, was high when either  $k_3$  (0.80) or  $K_1$  (0.86) values as calculated from 45-min dataset were used. These results suggest that single-session 45-min acquisitions in SCCHN patients may present an attractive alternative when used for identifying the presence of hypoxia on a tumor subvolume level.

Simulations were performed to assess uncertainties in  $^{18}\text{F}$ -fluoromisonidazole kinetic modeling due to statistical noise and shortened acquisition time. The decrease in %stddev of  $k_3$  with increasing  $k_3$  value is a possible result of the steeper rise in  $^{18}\text{F}$ -fluoromisonidazole uptake that allows a more precise estimation of  $k_3$ .  $K_1$  remained accurately estimated using shortened datasets, as observed in both patient and animal studies. As  $K_1$  is predominantly determined from the early parts of time–activity curves, the correlation between  $K_1$  as calculated using full versus shortened noisy time–activity curves was higher than the corresponding correlation for  $k_3$  (which strongly depends on the later parts of time–activity curves). No bias in  $K_1$  or  $k_3$  was observed when shortening the acquisition time, because kinetic modeling for shortened datasets was performed using truncated  $\text{mTAC}_{\text{FD}}$  and  $\text{IF}_{\text{FD}}$ . These results indicate that  $K_1$  and  $k_3$  could in principle be calculated accurately from shortened acquisitions. The discrepancy between simulation and clinical results, however, is due to the difference in the shape of time–activity curves as modeled using full or shortened datasets, which in turn highlights kinetic

**TABLE 4**  
Summary of Simulation Results

Kinetic rate constant	Metric	Full dataset (~170 min)	First shortened dataset (~100 min)	Second shortened dataset (45 min)
$k_3$	%bias	0.0 ± 0.1	0.0 ± 0.1	0.0 ± 0.2
	%SD	1.4 ± 0.7	2.0 ± 1.0	3.7 ± 2.0
	Pearson $r$ (range)		0.55 ± 0.08 (0.33–0.85)	0.19 ± 0.13 (0.00–0.80)
$K_1$	%bias	0.1 ± 0.1	0.1 ± 0.1	0.1 ± 0.1
	%SD	0.6 ± 0.2	0.6 ± 0.2	0.6 ± 0.2
	Pearson $r$ (range)		0.96 ± 0.10 (0.43–0.99)	0.93 ± 0.09 (0.48–0.99)

heterogeneity within tumor subvolumes as a potential source of bias (24,25). When the analysis in clinical studies was repeated using  $IF_{FD}$  for all datasets, the overestimation of  $k_3$  was not reduced (data not shown). The potential impact of misregistration between the 3  $^{18}F$ -fluoromisonidazole scans on overestimation of  $k_3$  (by means of combining tumor regions with different pharmacokinetic properties) is a subject of an ongoing study.

A limitation of this study was the small sample size. The used statistical methods do not address the clinical significance of the results. The clinical significance of differences between the kinetic rate constants as calculated from shortened and full dPET datasets has not yet been evaluated. Further, a test–retest study will be necessary to investigate the reproducibility of  $^{18}F$ -fluoromisonidazole kinetic modeling.

## CONCLUSION

Using single-session 45-min shortened  $^{18}F$ -fluoromisonidazole dPET datasets appears to be adequate for the identification of intratumor regions of hypoxia. However,  $k_3$  was significantly overestimated in the clinical cohort. Further studies are necessary to evaluate the clinical significance of differences between the results as calculated from full and shortened datasets.

## DISCLOSURE

The costs of publication of this article were defrayed in part by the payment of page charges. Therefore, and solely to indicate this fact, this article is hereby marked “advertisement” in accordance with 18 USC section 1734. This study was partially supported by NIH grants P30 CA008748, 5R01CA157770-04, and 5U01CA157442. No other potential conflict of interest relevant to this article was reported.

## REFERENCES

- Horsman MR, Mortensen LS, Petersen JB, Busk M, Overgaard J. Imaging hypoxia to improve radiotherapy outcome. *Nat Rev Clin Oncol*. 2012;9:674–687.
- Nordmark M, Overgaard M, Overgaard J. Pretreatment oxygenation predicts radiation response in advanced squamous cell carcinoma of the head and neck. *Radiother Oncol*. 1996;41:31–39.
- Brizel DM, Sibley GS, Prosnitz LR, Scher RL, Dewhirst MW. Tumor hypoxia adversely affects the prognosis of carcinoma of the head and neck. *Int J Radiat Oncol Biol Phys*. 1997;38:285–289.
- Rajendran JG, Schwartz DL, O’Sullivan J, et al. Tumor hypoxia imaging with [ $^{18}F$ ]fluoromisonidazole positron emission tomography in head and neck cancer. *Clin Cancer Res*. 2006;12:5435–5441.
- Nordmark M, Bentzen SM, Overgaard J. Measurement of human tumour oxygenation status by a polarographic needle electrode. An analysis of inter- and intratumour heterogeneity. *Acta Oncol*. 1994;33:383–389.
- Russell J, Carlin SD, Burke SA, Wen B, Yang KM, Ling CC. Immunohistochemical detection of changes in tumor hypoxia. *Int J Radiat Oncol Biol Phys*. 2009;73:1177–1186.
- Koh WJ, Rasey JS, Evans ML, et al. Imaging of hypoxia in human tumors with [ $^{18}F$ ]fluoromisonidazole. *Int J Radiat Oncol Biol Phys*. 1992;22:199–212.
- Rasey JS, Koh WJ, Evans ML, et al. Quantifying regional hypoxia in human tumors with positron emission tomography of [ $^{18}F$ ]fluoromisonidazole: a pretherapy study of 37 patients. *Int J Radiat Oncol Biol Phys*. 1996;36:417–428.
- Thorwarth D, Eschmann SM, Paulsen F, Alber M. A kinetic model for dynamic [ $^{18}F$ ]FMISO PET data to analyse tumor hypoxia. *Phys Med Biol*. 2005;50:2209–2224.
- Wang W, Lee NY, Georgi JC, et al. Pharmacokinetic analysis of hypoxia  $^{18}F$ -fluoromisonidazole dynamic PET in head and neck cancer. *J Nucl Med*. 2010;51:37–45.
- Lim JL, Berridge MS. An efficient radiosynthesis of [ $^{18}F$ ]fluoromisonidazole. *Appl Radiat Isot*. 1993;44:1085–1091.
- Bokacheva L, Kotedia K, Reese M, et al. Response of HT29 colorectal xenograft model to cediranib assessed with  $^{18}F$ -fluoromisonidazole positron emission tomography, dynamic contrast-enhanced and diffusion-weighted MRI. *NMR Biomed*. 2013;26:151–163.
- Wang W, Georgi JC, Nehmeh SA, et al. Evaluation of a compartmental model for estimating tumor hypoxia via FMISO dynamic PET imaging. *Phys Med Biol*. 2009;54:3083–3099.
- Rousset OG, Ma Y, Evans AC. Correction for partial volume effects in PET: principle and validation. *J Nucl Med*. 1998;39:904–911.
- Velamuru PK, Renaut RA, Guo H, Chen K. Robust clustering of positron emission tomography data. Paper presented at: Joint Conference of the Classification Society of North America and Interface Foundation of North America. June 8–June 12, 2005; St. Louis, Missouri.
- Press WH, Teukolsky SA, Wetterling WT, Flannery BP. *Numerical Recipes in C*. New York, NY: Cambridge University Press; 1992.
- Passing H, Bablok W. A new biometrical procedure for testing the equality of measurements from two different analytical methods: application of linear regression procedures for method comparison studies in clinical chemistry, Part I. *J Clin Chem Clin Biochem*. 1983;21:709–720.
- Bland JM, Altman DG. Statistical methods for assessing agreement between two methods of clinical measurement. *Lancet*. 1986;1:307–310.
- Zweig MH, Campbell G. Receiver-operating characteristic (ROC) plots: a fundamental evaluation tool in clinical medicine. *Clin Chem*. 1993;39:561–577.
- Schmidtlein CR, Beattie BJ, Bailey DL, et al. Using an external gating signal to estimate noise in PET with an emphasis on tracer avid tumors. *Phys Med Biol*. 2010;55:6299–6326.
- Eschmann SM, Paulsen F, Reimold M, et al. Prognostic impact of hypoxia imaging with  $^{18}F$ -misonidazole PET in non-small cell lung cancer and head and neck cancer before radiotherapy. *J Nucl Med*. 2005;46:253–260.
- Thorwarth D, Eschmann SM, Scheiderbauer J, Paulsen F, Alber M. Kinetic analysis of dynamic  $^{18}F$ -fluoromisonidazole PET correlates with radiation treatment outcome in head-and-neck cancer. *BMC Cancer*. 2005;5:152.
- Fleming IN, Manavaki R, Blower PJ, et al. Imaging tumour hypoxia with positron emission tomography. *Br J Cancer*. 2015;112:238–250.
- Herholz K, Patlak CS. The influence of tissue heterogeneity on results of fitting nonlinear model equations to regional tracer uptake curves: with an application to compartmental models used in positron emission tomography. *J Cereb Blood Flow Metab*. 1987;7:214–229.
- Schmidt K, Lucignani G, Moresco RM, et al. Errors introduced by tissue heterogeneity in estimation of local cerebral glucose utilization with current kinetic models of the [ $^{18}F$ ]fluorodeoxyglucose method. *J Cereb Blood Flow Metab*. 1992;12:823–834.
- Torizuka T, Nobezawa S, Momiki S, et al. Short dynamic FDG-PET imaging protocol for patients with lung cancer. *Eur J Nucl Med*. 2000;27:1538–1542.
- Monden T, Kudomi N, Sasakawa Y, et al. Shortening the duration of [ $^{18}F$ ]FDG PET brain examination for diagnosis of brain glioma. *Mol Imaging Biol*. 2011;13:754–758.
- Busk M, Munk OL, Jakobsen S, et al. Assessing hypoxia in animal tumor models based on pharmacokinetic analysis of dynamic FAZA PET. *Acta Oncol*. 2010;49:922–933.